Oil Spill Candidate Detection Using a Conditional Random Field Model on Simulated Compact Polarimetric Imagery

Saeid Taleghanidoozdoozan, Linlin Xu, and David A. Clausi

***Abstract*—Although the compact polarimetric (CP) synthetic aperture radar (SAR) mode of the RADARSAT Constellation Mission (RCM) offers new opportunities for oil spill candidate detection, there has not been an efficient machine learning model explicitly designed to utilize this new CP SAR data for improved detection. This paper presents a conditional random field model based on the Wishart mixture model (CRF-WMM) to detect oil spill candidates in CP SAR imagery. First, a "Wishart mixture model" (WMM) is designed as the unary potential in the CRF-WMM to address the class-dependent information of oil spill candidates and oil-free water. Second, we introduce a new similarity measure based on CP statistics designed as a pairwise potential in the CRF-WMM model so that pixels with strong spatial connections have the same class label. Finally, we investigate three different optimization approaches to solve the resulting maximum a posterior (MAP) problem, namely iterated conditional modes (ICM), simulated annealing (SA), and graph cuts (GC). The results show that our proposed CRF-WMM model can delineate oil spill candidates better than the traditional CRF approaches and that the GC algorithm provides the best optimization.**

***Index Terms*—RADARSAT Constellation Mission (RCM), synthetic aperture radar (SAR), compact polarimetry, spatial information, oil detection .**

I. Introduction

PROTECTING the environment is an important subject that has gained significant attention across the world. One of the most damaging events to the marine ecosystem is an oil spill which is usually caused by oil tanker accidents, illegal oily discharges from tank cleaning, or oil pipeline breakages [1]. As a result, detecting and cleaning up oil spills play an essential role in the lives of humans and marine life. The first step to efficiently reduce the destructive effects of oil spills on the environment is to detect oil spills accurately.

An appropriate choice to detect marine oil spills is to use synthetic aperture radar (SAR) systems because they can capture images of large areas, regardless of image acquisition time and weather conditions. The RADARSAT Constellation Mission (RCM) is Canada's newest generation of Earth observation SAR satellites launched in 2019 and consists of three satellites. The RCM data can be used for surveillance, disaster management, and environmental monitoring [2]. The RCM provides nearly daily coverage of Canada, and each satellite operates in single-polarization, dual-polarization (DP), and wide swath coverage compact polarimetric (CP) acquisition modes, as well as the quad-polarization (QP) mode [3]. The RCM CP SAR data has several benefits over the QP RADARSAT-2 SAR data, such as wide swath coverage and halved average transmitted power [4]. The RCM CP system has many advantages over the DP RADARSAT-2 SAR system such as minimum sensitivity to noise, cross-channel errors, self-calibration property, and providing more detailed information about objects[5]. However, compared to QP SAR, one of the main limitations of the CP SAR system is that it provides less polarimetric information, which might cause restrictions in complex problems such as oil slick characterization [6]. Furthermore, the number of SAR systems that operate in the CP mode is limited which may cause availability problems. Although CP SAR data suffers from these limitations, the advantages of the RCM CP SAR system over QP and DP RADARSAT-2 systems encourage researchers to use this type of SAR data.

Oil spill detection can be done manually by trained operators. In visual inspection methods, an expert has to examine the entire scene and identify oil spills [7]. Although a trained operator can identify oil spill candidates in a SAR image with sufficient certainty, processing SAR scenes by human analysts is difficult and time-consuming. Outputs generated from the visual inspection can vary since these are dependent on the knowledge and experience of operators. Therefore, designing automatic models to use SAR data for oil spill detection is essential for accurately detecting oil spills.

A number of natural phenomena can result in false oil spill detections such as marine organisms, shear zones, natural low wind zones (wind speed < 3 m/s), internal waves, rain cells, grease ice, and microconvective cells, which are known as oil spill look-alikes [8], [9]. The normalized radar cross section (NRCS) of look-alikes and oil spills are both low and similar; therefore, to separate them from each other with high accuracy, some important features such as wind speed, geometrical shapes, and backscattering characteristics should be used [10]. Under low wind conditions, separating oil spills from the surrounding calm ocean becomes difficult because each of these has a low backscatter [11]. The coherent interference of backscattered waves from many randomly distributed scatterers within a resolution cell causes bright and dark pixels in a radar image [12], [13]. This grainy salt-and-pepper noise is called speckle noise. An essential challenge in SAR oil spill candidate detection is caused by the speckle noise that creates low feature space separability between the oil spill and oil-free water classes. Generally, to reduce the effects of speckle noise, incoherent averaging using multiple looks or adaptive/non-adaptive signal processing filters are utilized [14]. Mixed pixels, containing both an oil spill candidate and water, are

usually found in SAR images with low spatial resolution, e.g., ScanSAR Wide mode with an approximate range $\times$ azimuth 100m nominal resolution. The mixed pixels lead to an increase in oil spill detection error.

There are a limited number of published papers on the subject of oil spill detection using CP SAR data [15–18]. Previous studies have not used the statistical distribution of CP SAR data in oil spill detection applications. Therefore, one of the main contributions of this paper lies in incorporating statistical properties of CP SAR data to identify oil spill candidates. Context is an important information source in analyzing SAR data. In this paper, the spatial context information in SAR imagery is used to improve class separability. We introduce a model based on a conditional random field (CRF) which reduces the destructive effects of speckle noise and highlights the difference between oil spills and oil-free water by effectively modeling the spatial contextual information. The CRF consists of the unary and pairwise potentials. The unary potential utilizes the statistical properties of individual pixels, while the pairwise potential represents relationships between neighboring pixels [19], [20]. Nevertheless, a CRF is traditionally built upon SAR intensity images, and we are not aware of a CRF model designed to address the statistical properties of the complex CP SAR data. The second aim of this paper is to introduce a similarity measure based on CP SAR data to better model spatial contextual information. Since solving the CRF is an ill-posed problem, an optimization algorithm needs to be used to obtain the optimum result. Therefore, the third and last aim of this paper is to assess the performance of optimization algorithms so that the resulting CRF model can be tailored to the characteristics of the CP SAR data for dealing with the future RCM CP SAR data in oil spill candidate detection applications.

In summary, the contributions of this paper lie in the following aspects. First, a Wishart mixture model (WMM) based on the complex Wishart distribution is designed to implement the CRF-WMM's unary potential to accommodate the discriminative class statistics in the CP SAR data. Second, the pairwise potential in CRF-WMM is implemented using a similarity measure based on the CP statistics to leverage spatial correlation. Finally, we identify the best approach for solving the resulting CRF-WMM model of the three popular optimization approaches.

The remainder of this paper is organized as follows: Section II reviews related work and Section III describes the structure of CP SAR data. Section IV explains the details of the methodology. Then, after introducing the study area in Section V, Section VI presents the results. The last section concludes the study.

II. Related work

Early research on SAR oil spill detection was conducted using single-polarization SAR data, generally using the VV(vertical transmit, vertical receive) polarization [21]. Elachi [22] is recognized as the first to use SAR data to monitor oil spills using data from the Seasat satellite. The enhanced capabilities of the second generation of satellite SAR sensors such as ENVISAT, RADARSAT-1, and ERS-2 attracted further attention for oil spill monitoring [23–25]. Xu *et al* [26] performed a comprehensive study of different classification techniques to detect oil spills using ninety-three RADARSAT-1 ScanSAR Narrow Beam images. They utilized fifteen features and different classification methods to distinguish oil spills from look-alike phenomena.

The third generation of SAR sensors, such as the Canadian RADARSAT-2 and German TerraSAR-X, offer QP SAR modes, higher spatial resolution and shorter revisit times than previous SAR missions [27], [28]. With the availability of QP SAR data, researchers have also explored QP SAR data for oil spill selection [17], [29], [30]. Minchew *et al* [11] investigated $H/A/\alpha$ eigenvector decomposition parameters extracted from QP UAVSAR (uninhabited aerial vehicle SAR) data to analyze the backscattering of the Deepwater Horizon (DWH) oil spill and determined that the major eigenvalue of the coherency matrix was the most promising indicator for oil slick detection. Genovez *et al* [31] proposed a multi-source approach to utilize optical, single-channel SAR, and QP SAR data to distinguish oil from water and classify oil into two thick and thin layers. Espeseth *et al* [6] used a series of short time revisit SAR images to identify areas with relatively thick oil slicks. Their results showed that multiple SAR images with short repeat times could provide new information to identify short term oil slick drifts, which is important for clean up efforts. Skrunes *et al* [32] investigated the discrimination potential of the eight well-known multipolarization features by measuring between-region contrast and within-region variance and concluded that the pair of geometric intensity and the real part of the copolarization cross product features could be used to determine the most promising results.

Several approaches have been proposed for oil spill candidate detection by taking advantage of spatial contextual information. One method is to employ a graphical model. Xu *et al* [33] introduced a stochastic fully connected CRF based on a Gaussian mixture model (GMM) to detect dark spots on RADARSAT-1 images, demonstrating that incorporating spatial information can improve results. Morales *et al* [34] utilized a hierarchical Markov random field (MRF) to segment SAR images into oil classes (denser and thinner) and sea water. Pelizzari and Bioucas-Dias [35] used an MRF based on graph cuts to detect oil spills in SAR intensity images. Martinis [36] used a hybrid Markov image model by integrating scale-dependent and spatial context information into the labeling process for near real-time oil spill detections in high-resolution TerraSAR-X ScanSAR data. Parmiggiani *et al* [37] used a threshold GMM-MRF model to segment oil spills in a SAR image. Other mathematical tools which utilize spatial relationships among pixels are convolution neural networks (CNNs). De Laurentiis *et al* [9] utilized a CNN to separate mineral films from biogenic slicks and the oil-free sea surface. Guo *et al* [38] employed a CNN to discriminate oil spills from look-alikes, while Yaohua and Xudong [39] used a dense connected CNN for the same task.

There are a limited number of published papers on oil spill detection using CP SAR data. Zhang *et al* [15] extracted the conformity coefficient from simulated hybrid-polarity (HP) CP

SAR data [5] from QP RADARSAT-2. They applied it along with entropy and the average alpha angle to detect oil spills. Salberg *et al* [18] proposed a coherence measure, which relies on the Bragg scattering assumption, to detect oil spills in simulated HP SAR data obtained from RADARSAT-2 data. They compared the performance of their proposed measure with the degree of polarization (DoP), the conformity coefficient, and the correlation coefficient. According to their results, the coherence measure suppresses some look-alikes caused by low wind. Nunziata *et al* [17] investigated features extracted from HP SAR data based on sea surface scattering with or without oil spills. Moreover, they proposed a new measure called the standard deviation of the phase difference (σ), where the value of σ for oil-covered surfaces is larger than that for slick-free regions. Li *et al* [40] proposed a new method to retrieve the mixture ratio of oil and water in CP SAR data by using the diagonal elements of the covariance matrix of CP SAR data. In [41], an iterative reconstruction QP SAR image method using CP SAR data based on the different statistical behavior between oil spills and open sea surface was proposed. Shirvany *et al* [16] investigated the potential use of DoP calculated for CP and DP SAR data to detect ships and oil spills. Their experiment showed that using the HP CP mode and DP (HH, VV) modes result in better detection performance. Espeseth *et al* [42] compared the performance of a set of features extracted from QP UAVSAR and simulated HP SAR data under a high wind situation, and concluded that the capability of the HP data to distinguish different slicks from each other as well as from oil-free water is comparable with that of the QP data. Collins *et al* [21] investigated the potential of the reconstructed QP SAR data based on CP SAR data to create the oil/water mixing index called Mdex [43]. According to their results, pseudo-QP SAR and QP SAR data resulted in similar Mdex maps. Chaudhary and Kumar [44] investigated the potential of using decomposition parameters extracted from QP UAVSAR (uninhabited aerial vehicle SAR) and CP RISAT-1 SAR images for detecting oil slicks. Here, using Van Zyl parameters [45] achieved the best results for the UAVSAR dataset, and utilizing compact-pol decomposition parameters [46] achieved the best results for the RISAT-1 dataset. A study by Chaudhary and Kumar [47] investigated the capability of using features measured from QP and simulated HP imagery to distinguish oil spills from oil-free water. Classification using HP features achieved an accuracy of more than 98%. Li *et al* [48] analyzed the polarimetric properties of oil-covered ocean surface water in CP SAR data using the polarimetric degree m and the Poincar ellipticity χ parameters [5], [49] They concluded that the sign of χ is opposite for the oil spills from oil-free water. Moreover, compared to oil-free water, oil spills reduce the value of m.

Most of the methods described above have been applied to detect oil spills by utilizing pixel-based features. However, single-pixel measurements are strongly affected by speckle noise resulting in noisy outputs [50], [51]. In this paper, we consider spatial context information to reduce speckle effects and the impact of intra-class variations to increase class separability for the oil spill detection problem. Moreover, in contrast to previous studies such as [33], [52], we investigate the use of a more appropriate statistical model to include in a CRF model that is better able to more accurately detect oil spill candidates in CP SAR data.

III. Compact polarimetric SAR basics

The architectures of CP SAR can be classified into three modes [53]: (i) $\frac{\pi}{4}$, (ii) circular-circular (CC), and (iii) HP. The RCM consists of three identical SAR satellites that operate in C-band and HP mode. In the HP mode, a circular polarization is transmitted, and both H and V polarizations are received.

The coherency matrix of CP SAR data is a 2×2 semi-positive definite Hermitian matrix. For an HP mode in which a right circular polarized wave (R) is transmitted, and coherent dual linear H and V polarizations are received, known as the CTLR mode, the coherency matrix C_{CTLR} is given as:

$$\mathbf{C}_{CTLR} = \begin{bmatrix} \langle \mid S_{RH}^2 \mid \rangle & \langle S_{RH} S_{RV}^* \rangle \\ \langle S_{RV} S_{RH}^* \rangle & \langle \mid S_{RV}^2 \mid \rangle \end{bmatrix} \tag{1}$$

where S_{ij} indicates a complex element of the scattering matrix. $\langle ... \rangle$ defines spatial ensemble averaging and * indicates the conjugate transpose. The diagonal elements (real numbers) describe the intensities and the non-diagonal (complex numbers) describe the intensities and phase between polarizations. Due to the limited CP SAR data available, a popular method to obtain C_{CTLR} is to simulate it from given QP data [54]. The covariance matrix for the CTLR mode can be written as [55–57]:

$$\begin{aligned} \mathbf{C}_{CTLR} &= \frac{1}{2}\begin{bmatrix} \langle \mid S_{HH} \mid^2 \rangle & j\langle S_{HH} S_{VV}^* \rangle \\ -j\langle S_{VV} S_{HH}^* \rangle & \langle \mid S_{VV} \mid^2 \rangle \end{bmatrix} + \frac{\langle \mid S_{HV} \mid^2 \rangle}{2}\begin{bmatrix} 1 & -j \\ j & 1 \end{bmatrix} \\ &\quad + \frac{1}{2}\begin{bmatrix} -2Im\langle S_{HH} S_{HV}^* \rangle & \langle S_{HH} S_{HV}^* + S_{VV}^* S_{HV} \rangle \\ \langle S_{HH}^* S_{HV} + S_{VV} S_{HV}^* \rangle & 2Im\langle S_{VV} S_{HV}^* \rangle \end{bmatrix} \\ &= \begin{bmatrix} C^{11} & C^{12} \\ C^{21} & C^{22} \end{bmatrix} \end{aligned} \tag{2}$$

where Im indicates the imaginary part of a complex number.

In some studies, such as [58], it has been assumed that the intensities of pixels follow a Gaussian mixture distribution. Multi-look processing is performed by averaging several single-look images to reduce speckle noise and compress SAR data [59], [60]. An L-look SAR intensity image, in which L indicates the number of looks, is known to have a gamma distribution [61]. The coherency matrix follows a complex Wishart distribution [62]. This property of the coherency matrix is used by other machine learning methods which are applied to polarimetric SAR data [44], [63], [64]

IV. Methodology

A. CRF-WMM framework

Let S represent the discrete two-dimensional rectangular lattice and $i \in S$ be a site in the lattice (i.e., a pixel in the image). A CP SAR image is represented by $Y = \{y_i | i \in S\}$, where Y is a random field on S. Moreover, $X = \{x_i | i \in S\}$ is a set of binary-valued random variables which form a random field on S. For oil spill candidates $x_i = 1$, oil free water $x_i = 0$. Based on this formulation, the task of oil spill candidate

detection from CP SAR imagery aims to estimate X bases on Y, which is achieved using a novel CRF-WMM model that addresses both the backscattered information and the spatial context information in the CP image.

The proposed CRF-WMM model addresses the posterior probability distribution of the label map X given the CP SAR imagery observation Y by [33]:

$$p(X|Y) = \frac{1}{Z(X)} exp\{-\sum_{i\in S} \psi_u(x_i,y_i) - \beta \sum_{i\in S}\sum_{j\in N_i} \psi_p(x_i,x_j,y_i,y_j)\} \tag{3}$$

in which $Z(X)$ is a normalization factor called the partition function. ψ_u and ψ_p are the unary potential and the pairwise potential, respectively, and β dictates the relative weight of the two potentials. N_i denotes a set of 4 neighbors of pixel i. Given this formulation, the estimation of X is achieved by maximizing $p(X|Y)$ under the maximum a posterior (MAP) framework. The CRF-WMM model can be solved by addressing the following MAP problem:

$$\hat{X} = arg\max_X(p(X|Y)) \tag{4}$$

To identify the most appropriate optimization method to solve Equation (4), three well-known methods, i.e., iterated conditional modes (ICM) [65], simulated annealing (SA) [66], and graph cuts (GC) [67] are compared.

B. CP Unary Potential via WMM

The unary potential ψ_u in CRF-WMM is calculated by taking into consideration the statistical distribution of the CP SAR data. The unary potential in the CRF model is used to address the class-dependent information of different classes and is defined as:

$$\psi_u(x_i,y_i) = -ln(p(x_i|y_i)) \tag{5}$$

where $p(x_i|y_i)$ is designed based on the statistical characteristics of the data. To achieve this, a GMM is typically used [33], [52]. However, because the coherency matrix in Equation (2) follows a complex Wishart distribution [68], a new mixture model based on the Wishart distribution is proposed.

The ith pixel in CP SAR imagery is represented by a complex matrix $A_i = LC_i$. Because C_i follows a complex Wishart distribution, the class-dependent distribution of A_i given C_{x_i} has the following expression:

$$p(A_i|C_{x_i}) = \frac{|\,A_i\,|^{L-q}\, exp(-tr(C_{x_i}^{-1}A_i))}{K(L,q)\,|\,C_{x_i}\,|^{L}} \tag{6}$$

where C_{x_i} is the average of the covariance matrices of pixels from class x_i. The symbols $|\,.\,|$ and tr denote the determinant and trace operations, respectively. Moreover $K(L,q)$ is defined as:

$$K(L,q) = \pi^{\frac{1}{2}q(q-1)} \prod_{r=1}^{q} \Gamma(L-r-1) \tag{7}$$

in which q is the number of elements in the complex scattering vector and Γ is the Gamma function. By substituting Equation (6) into Equation (3), the unary potential for the complex Wishart distribution is represented as:

$$\begin{aligned}\psi_u(x_i,y_i) = Lln\,|\,C_{x_i}\,| + ln(K(L,q)) + \\ tr(C_{x_i}^{-1}A_i) - (L-q)ln(|\,A_i\,|)\end{aligned} \tag{8}$$

After substituting $A_i = LC_i$ into Equation (8) and eliminating elements that are not a function of x_i, the unary potential in CRF-WMM will be:

$$\psi_u(x_i,y_i) = ln\,|\,C_{x_i}\,| + tr(C_{x_i}^{-1}C_i) \tag{9}$$

C. CP pairwise potential

The pairwise potential ψ_p in Equation (3) represents the relationships between the labels and the features of neighbouring pixels. ψ_p in CRF-WMM is defined by a new similarity measure designed based on the properties of CP SAR data. ψ_p has been implemented using the following expression:

$$\psi_p(x_i,x_j,y_i,y_j) = \lambda(y_i,y_j).\mu(x_i,x_j) \tag{10}$$

where $\mu(x_i,x_j)$ is considered as the multi-level logistic (MLL) model [69], and $\lambda(y_i,y_j)$ is a measure of feature similarity. Designing a $\lambda(y_i,y_j)$ in ψ_p for CP data is necessary to achieve the best performance since doing so can more effectively constrain pixels with a strong spatial correlation to have the same class label while also reducing the effects of noise and spatial heterogeneity in SAR imagery leading to more accurate predictions.

The similarity measure $\lambda(y_i,y_j)$ in Equation (10) returns a larger value for two pixels with a stronger spatial correlation. Although a metric defined based on the full CP information theoretically can better reveal the similarity among pixels, using all elements in the covariance matrix in Equation (2) will increase the computational burden. We choose C^{22} because it is suitable for oil spill detection due to its higher signal-to-noise ratio and sensitivity to the sea surface roughness [70]. Therefore, a similarity measure is designed based on the C^{22} elements given in Equation (2):

$$\lambda(C_i^{22},C_j^{22}) = exp(\frac{-\,|\,C_i^{22}-C_j^{22}\,|^2}{2\theta^2}) \tag{11}$$

where θ controls the scale of the Gaussian kernel. $\lambda(C_i^{22},C_j^{22})$ generates high values if $|\,C_i^{22}-C_j^{22}\,|^2$ is small; therefore, $\lambda(C_i^{22},C_j^{22})$ constrains pixels with similar values to each have the same class label. By substituting Equation (11) in Equation (10), the pairwise potential in CRF-WMM will be:

$$\psi_p(x_i,x_j,y_i,y_j) = exp(\frac{-\,|\,C_i^{22}-C_j^{22}\,|^2}{2\theta^2}).(1-\delta(x_i,x_j)) \tag{12}$$

D. Optimization approaches

Solving the CRF is an ill-posed problem; therefore, an optimization algorithm is necessary to solve it. To assess the variety of optimization algorithms, it is necessary to evaluate their performance in oil spill candidate detection by using CP SAR data. The MAP problem in Equation (4) can be reformulated as:

$$\hat{X} = arg\min_X(-ln(p(X|Y))) \tag{13}$$

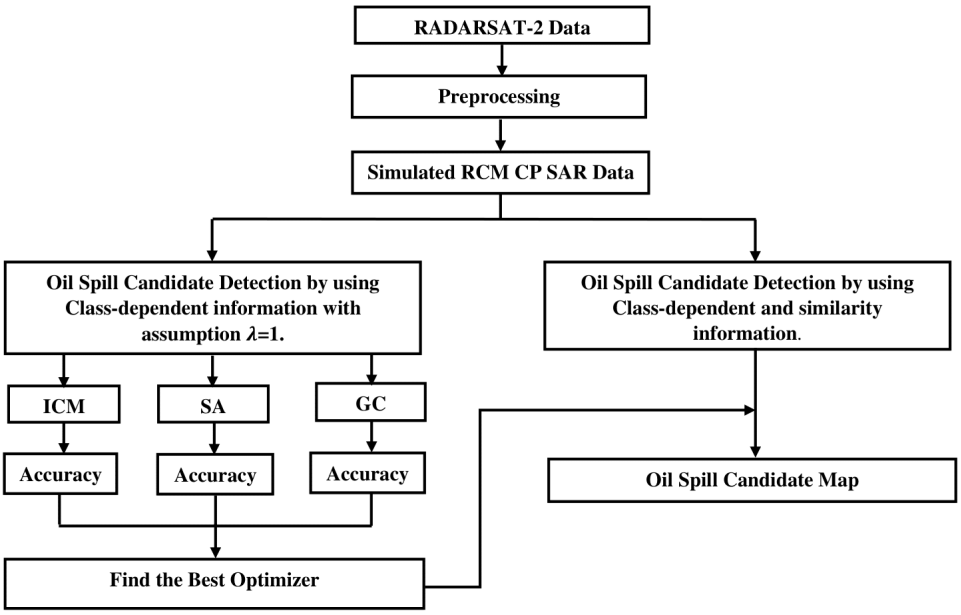

Fig. 1: The flowchart of the proposed method to detect oil spill candidates from simulated RCM CP SAR data.

By substituting the unary potential (Equation (9)) and the pairwise potential (Equation (12)) into Equation (13), the MAP problem can be expressed as:

$$\hat{X} = arg\min_{X}\{\sum_{i\in S}(ln \mid C_{x_i} \mid + tr(C_{x_i}^{-1}C_i)) + \beta\sum_{i\in S}\sum_{j\in N_i} exp(\frac{-\mid C_i^{22} - C_j^{22} \mid^2}{2\theta^2}).(1-\delta(x_i,x_j))\} \quad (14)$$

The parameter to be estimated, $\hat{X}$, is a binary variable. So, Equation (14) defines a combinatorial optimization problem, which can be solved by several techniques. In this study, we investigate and compare ICM, GC, and SA as optimization methods to obtain $\hat{X}$.

E. Summary of the Proposed Model

Fig. 1 illustrates the flowchart of the proposed model to detect oil spill candidates. Below we provide a summary of the CRF-WMM model which is a thresholding guided segmentation approach. Given a CP SAR image Y, the following steps are performed:

1) Perform binary thresholding on C^{22} from Y to obtain an initial estimation of X, and use this estimate to calculate the class probabilities for oil-free water C_0 and oil spills C_1.
2) Calculate the unary potential as per Equation (9).
3) Calculate the pairwise potential based on the similarity measure as per Equation (12).
4) Calculate the objective function as per Equation (14), and solve it using each optimization technique (i.e., ICM, GC, and SA).

V. Study Area

In this study, the potential of the proposed model in detecting oil spill candidates is investigated by using simulated RCM CP SAR images. To simulate RCM CP SAR images, three QP RADARSAT-2 images acquired over Coal Oil Point, near Santa Barbara, California, USA are used. The details of the RADARSAT-2 images are represented in Table I. These images have been provided by the Canadian Ice Service (CIS) under the Integrated Satellite Tracking of Pollution (ISTOP) program [71]. To simulate CP SAR data, the RCM CP simulator is used. This simulator was developed at the Canada Centre for Mapping and Earth Observation (CCMEO) [72]. Data was simulated for the RCM medium resolution beam mode with 50 m range $\times$ 50 m azimuth nominal resolution and -22 dB noise floor (noise-equivalent sigma zero (NESZ) value). A 9$\times$9 boxcar filter was applied to all the scenes to reduce the effects of speckle noise. A consequence of NRCS values lower than the NESZ is the loss of information. Although utilizing spatial context information and the coherency matrix of CP SAR data along with an appropriate statistical model make the proposed model able to distinguish oil spill candidates from oil-free water with NRCS above the NESZ, characterizing oil spills for NRCS values lower than -22 dB may not be possible [42].

Figure 2 shows the location and Pauli color composite of Scene 20090919. Features of a single pixel are affected by speckle noise and this makes the automated detection of oil spills more challenging. Models which only use single-pixel features without spatial context information as input cannot classify these types of oil spill candidates effectively. Therefore, an appropriate statistical model needs to be used, in which the spatial relationship between pixels should be utilized to detect boundaries and regions of oil spills. Thus, this paper uses a CRF model based on the complex Wishart distribution which takes advantage of the complex terms in the coherency matrix as well as spatial context information.

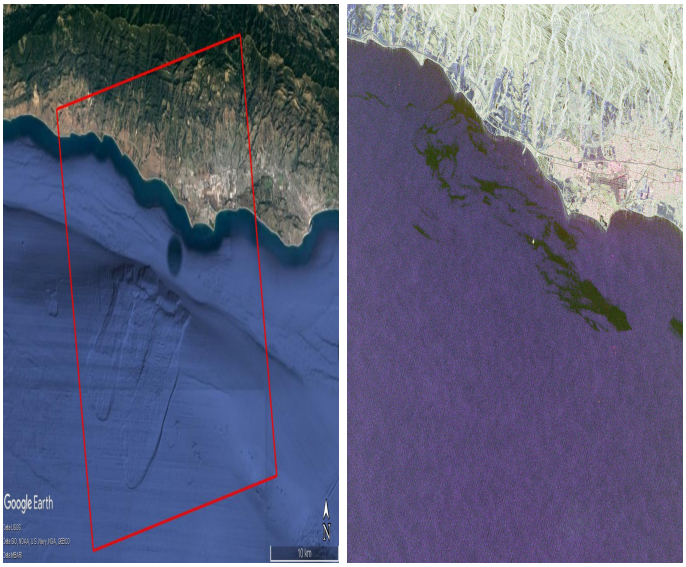

((a)) ((b))

Fig. 2: (a) Location of Scene 20090919, near Santa Barbara, California, USA. (b) The Pauli decomposition of Scene 20090919 with $|S_{HH}-S_{VV}|$, $|S_{HH}+S_{VV}|$, and $2|S_{HV}|$.

TABLE I: The details of the Fine Quad (FQ) single look complex RADARSAT-2 imagery used to simulate CP SAR data. The first column shows the date of acquisition in the format YearMonthDay. The first two images are used to simulate sub-images and the last image is used to simulate a full scene.

Scene	Beam	Range (m)	Azimuth (m)
20100131	FQ6	4.73	4.70
20100224	FQ6	4.73	4.70
20090919	FQ18	4.73	4.95

VI. Experiment and Discussion

This section presents the results obtained by the proposed method using the simulated RCM CP SAR sub-images of different sizes and a simulated RCM CP SAR full scene. Moreover, the performance of the optimization algorithms is compared in this section.

A. Quantitative Measures

In our experiments, ground truth data is generated based on visual inspection. To evaluate the performance of the proposed model, we use the following error metrics [33]:

- Commission error (CE) is defined as the ratio of the number of false predicted oil spill candidate pixels to the number of all predicted oil spill candidate pixels. CE is calculated as follows:

$$CE = \frac{A_E - A_T}{A_E} \tag{15}$$

where A_E denotes the number of all predicted oil spill candidate pixels and A_T denotes the number of pixels which are correctly classified as oil spill candidates.

- Omission error (OE) is defined as the ratio of the number of false predicted oil-free water pixels to the number of all ground truth oil spill candidate pixels. OE is calculated as follows:

$$OE = \frac{A_R - A_T}{A_R} \tag{16}$$

where A_R indicates the total number of ground truth oil spill candidate pixels.

- Averaged error (AE) is the average of CE and OE. AE measures the balanced detection capability of different methods and it is defined as:

$$AE = \frac{C_E + O_E}{2} \tag{17}$$

In this study, we use a grid search on C^{22} to find the best values for β and θ in Equation (14). Both parameters are varied from 0.5 to 5 in increments of 0.5, and the result with the lowest AE is chosen as the output of each method.

B. Experiment with Sub-images

Since oil spills are rare phenomena and usually appear in only small sections of a scene, models are usually tested using a sub-image containing oil spills. Therefore, to evaluate the performance of the proposed method, we use the two simulated scenes to extract five sub-images of different sizes (See Table I).

Because the CRF-WMM model consists of three building blocks, i.e., the unary potential, the pairwise potential, and the optimization algorithm, we use ablation experiments to isolate their roles and test their importance. First, to justify our unary potential, we compare the proposed WMM with the GMM model built on a vector of C^{11}, $abs(C^{12})$, and

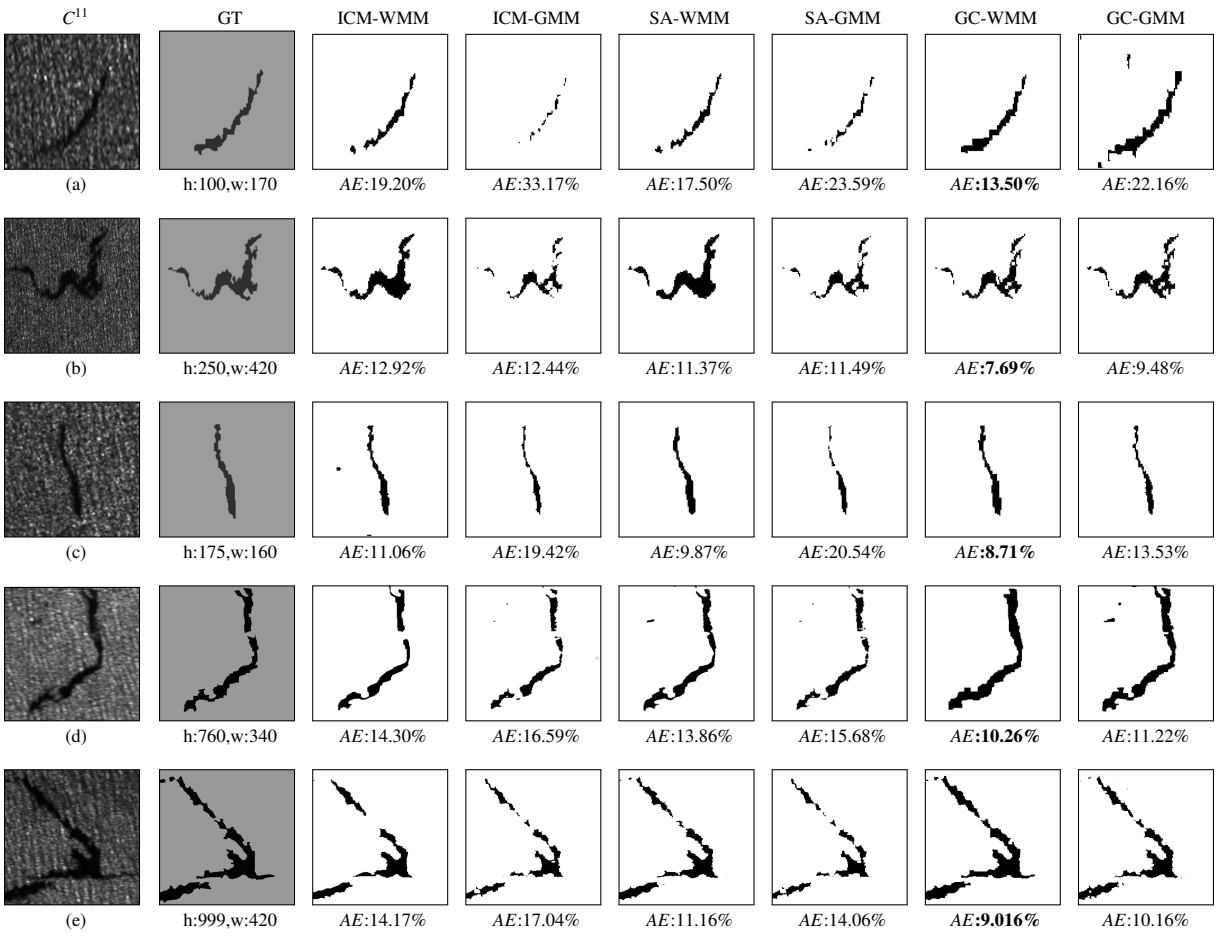

Fig. 3: Detected oil spill candidates by using the Wishart mixture model (WMM) and Gaussian mixture model (GMM) as the unary potential with different optimization methods and the assumption that $\lambda(C_i^{22}, C_j^{22}) = 1$. The first column shows the five data sets. The second column shows the ground truth (GT) data generated manually based on visual inspection. The h and w stand for the number of pixels in height and width of the sub-images, respectively. Numbers in **bold** indicate the lowest average error (*AE*) in each sub-image.

C^{22}. That is a common approach [33], [52], [58]. Second, to justify the use of the pairwise potential in the CRF-WMM over the traditional isotropic homogeneous MRF model commonly used [35], [52], we compare the proposed pairwise potential with an MRF potential implemented by discarding the similarity measure $\lambda(y_i, y_j)$ in Equation (10) and only use $\mu(x_i, x_j)$. In this experiment, we also compare different optimization methods to identify the one which achieves the highest accuracy.

1) Unary Potential and Optimization Approaches: Figure 3 shows the results of different methods, i.e., the combination of different unary implementations (GMM vs. WMM) and the different optimizers (ICM, SA, and GC). Regardless of the optimization techniques used, the GMM model tends to incorrectly classify oil spill candidate pixels as oil-free water. However, WMM is able to reduce the number of false negatives. This is because the phase information helps the model more appropriately characterize the statistical behaviour of RCM CP SAR data. Table II shows the mean values of *CE*, *OE*, and *AE* of the five sub-images by using the different methods. The WMM-based methods achieve much lower *OE* than the corresponding GMM-based methods. Low *OE* is more important than low *CE* for oil spill candidate detection problems because omitted potential oil spills will never be detected in the further classification of the true oil spills and the look-alikes. These results demonstrate the importance and improvements of using the proposed WMM approach for implementing the unary potential in the CRF model.

TABLE II: Mean values of the errors for the sub-images achieved by WMM and GMM unary potentials using the different optimization methods.

	CE(%)	*OE*(%)	*AE*(%)
ICM-WMM	11.46	17.20	14.27
ICM-GMM	**1.44**	38.02	19.81
SA-WMM	11.32	14.97	12.75
SA-GMM	2.83	31.53	17.18
GC-WMM	14.04	**5.63**	**9.83**
GC-GMM	18.09	9.40	13.31

Numbers in **bold** indicate the lowest error using each of the optimization methods

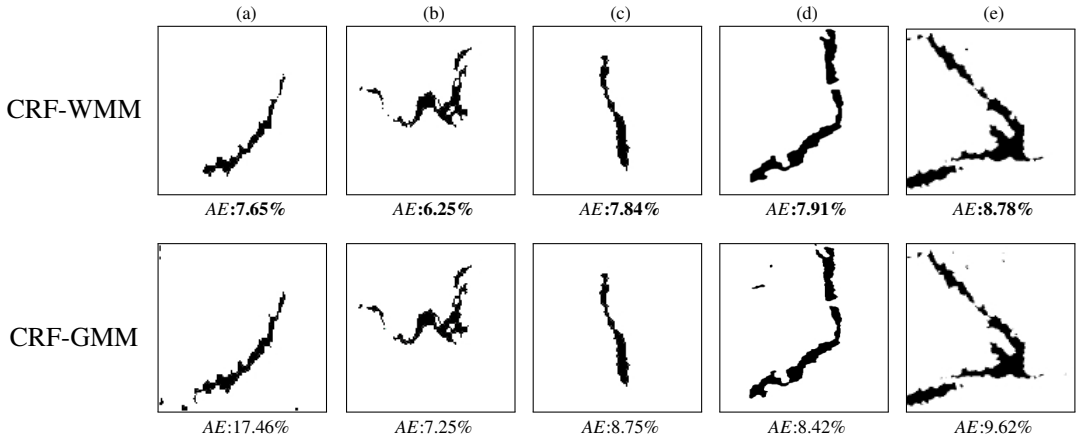

Fig. 4: Oil spill candidates detected by using the CRF-WMM and CRF-GMM models using the GC optimizer along with their *AE*. The first and second rows show the results obtained by the CRF-WMM and CRF-GMM models, respectively. Each column shows the sub-images. Numbers in bold indicate the lowest *AE* in each sub-image

Comparing the performance of the optimization algorithms, SA outperforms ICM. We hypothesize that this is because the solution for ICM is known to routinely became trapped in a local minimum [73]. However, SA employs a random search scheme to overcome this problem. Although utilizing GC increases *CE*, it significantly reduces *OE* in both WMM and GMM models. We expect this is due to the fact that GC is able to preserve relevant sharp discontinuities while enforcing the piecewise smoothness [74].

2) Pairwise Potential : In Subsection VI-B1, pairwise potentials were considered, which depend only on the labels of neighboring pixels, while the similarity among features of pixels was ignored. Moreover, the benefits and improvement of using the proposed WMM approach over GMM for implementing the unary potential in the CRF model was demonstrated, and GC was identified as the optimizer that achieved the highest accuracy. This experiment further demonstrates the role and importance of the similarity measure $\lambda(y_i, y_j)$ defined in Equation (11) by incorporating it into the previous GC-GMM and GC-WMM models. Figure 4 shows the results obtained by the CRF-WMM model and the baseline CRF-GMM model on the five sub-images using the GC optimizer. The similarity measurement assists the model in preserving the boundaries with higher accuracy by removing wrongly classified pixels. This effect of the similarity measurement is more noticeable for the first, third, and fourth data sets (Figure 3 (a, c, d) and Figure 4 (a, c, d)). Moreover, employing the feature similarity among neighborhood pixels reduces the number of false positives. For example, some dark areas were classified wrongly as oil spill candidates by GC-GMM in the first dataset but applying $\lambda(y_i, y_j)$ assigns them to the correct class label.

Table III illustrates the statistics achieved by CRF-WMM and CRF-GMM on the five sub-images. As expected, the performance of the proposed method in all data sets is better than that of CRF-GMM. Compared to the results presented in Table II, there is a significant reduction in the mean values of *CE*. Specifically, the error is reduced from 14.04% using GC-WMM to 9.04% using CRF-WMM and from 18.09% using GC-GMM to 13.46% using CRF-GMM. This confirms that using $\lambda(y_i, y_j)$ for implementing the pairwise potential in the CRF model reduces the number of false positives. Moreover, CRF-GMM improves *OE* by about 2%, while CRF-WMM increases *OE* by about 0.5%. Comparison of the results in Figure 3 with those in Figure 4 demonstrates consistency with the quantitative measures presented in Table III.

TABLE III: Mean values of the errors for the sub-images achieved by CRF-WMM and CRF-GMM using the GC optimization method.

	CE(%)	*OE*(%)	*AE*(%)
CRF-WMM	**9.04**	**6.29**	**7.68**
CRF-GMM	13.46	7.13	10.30

Numbers in **bold** indicate the lowest error using each of the optimization methods

C. Experiment with a Simulated CP SAR Full Scene

To show that the proposed method can reliably detect oil slicks, we examined the performance of the proposed model over a full scene. We used Scene 20090919 to simulate an RCM CP SAR scene. Figure 5 (a) illustrates the C^{11} image of the study area. It contains three classes, namely, open water, oil spill candidate, and land area. However, since the problem is a two-class classification, a mask is used to exclude the land areas from the calculation. Figure 5 (b) shows the manually generated ground truth oil spill candidate data.

Figure 6 shows the results obtained by the different methods and optimization algorithms. As expected, the performance of WMM on the simulated scene of CP SAR data is better than that of GMM. The results obtained by the GMM-based methods are less accurate due to more false positive being detected compared to the WMM-based methods, specially closer to the coastline. Among WMM-based methods, the ICM-WMM method tends to blur the boundaries by accepting pixels close to the boundaries as oil spill candidates. The SA-WMM and GC-WMM methods effectively identify oil-free water even when the backscatter of the open water has

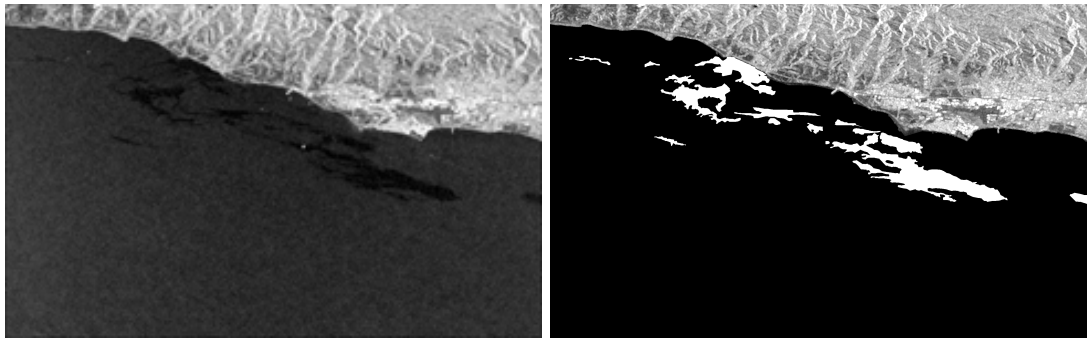

(a) (b)

Fig. 5: (a) 50 m resolution RADARSAT Constellation Mission right-horizontal polarization imagery (C^{11}) of an area near Santa Barbara simulated from data acquired on 19 September 2009. (b) Ground truth data of oil spill candidates generated manually based on visual inspection.

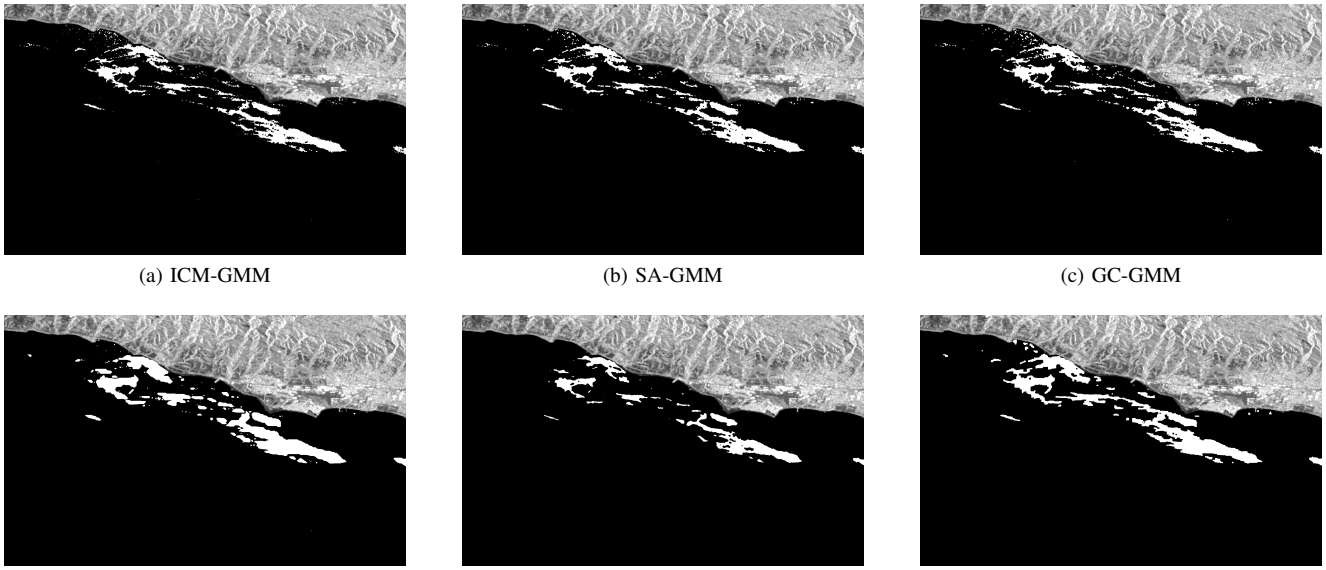

(a) ICM-GMM (b) SA-GMM (c) GC-GMM

(e) ICM-WMM (f) SA-WMM (g) GC-WMM

Fig. 6: Oil Spill candidate detection based on the WMM and GMM unary potentials by using the different optimization methods and assumption that $\lambda(C_i^{22} - C_j^{22}) = 1$.

high variability. This is because, compared to GMM-based methods, they utilize a more appropriate statistical model. Table IV indicates the errors obtained by the proposed and baseline GMM methods. An examination of Table IV shows that the values of *OE* obtained by WMM-based methods are much lower than those obtained by GMM-based ones. A high rate of *CE* causes a high computational cost in removing look-alike candidates. Thus, the capability of a model to produce a balanced *OE* and *CE* error is also important. Compared to GMM-based methods, WMM-based methods reach lower *AE*. This confirms the balanced detection capability of the proposed model. Moreover, as per the results in Subsection VI-B, the accuracy of the models using GC is higher than that of the other optimization algorithms. In the next experiment, the performance of CRF-WMM and CRF-GMM on the simulated full scene is evaluated. Since GC achieves a higher accuracy for oil spill detection than the other algorithms, the GC optimization method is used.

TABLE IV: Mean values of the errors for the sub-images achieved by WMM and GMM unary potentials using the different optimization method.

	CE(%)	*OE*(%)	*AE*(%)
ICM-WMM	23.15	9.54	16.34
ICM-GMM	**4.94**	31.87	18.41
SA-WMM	14.34	13.11	13.73
SA-GMM	6.06	24.11	15.07
GC-WMM	13.85	**9.08**	**11.58**
GC-GMM	12.72	16.44	14.58

Numbers in **bold** indicate the lowest error using each of the optimization methods

Figure 7 illustrates the results obtained by CRF-WMM and CRF-GMM. Visually, the similarity measure reduces the number of misclassified pixels in both CRF-WMM and CRF-GMM. Furthermore, CRF-GMM achieves a smaller number of false positives. The statistics of the numerical measures

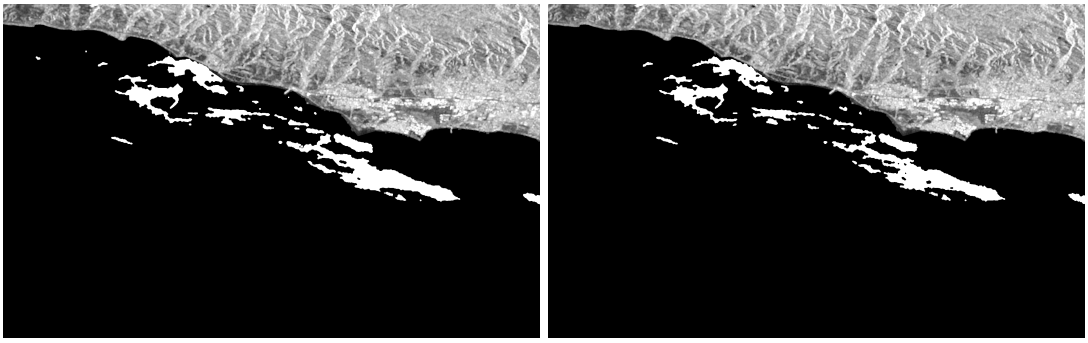

(a) CRF-WMM (b) CRF-GMM

Fig. 7: Detected oil spill candidates by using (a) the CRF-WMM model with $AE = 9.56\%$ and (b) the CRF-GMM with $AE = 11.29\%$. GC is used as the optimizer.

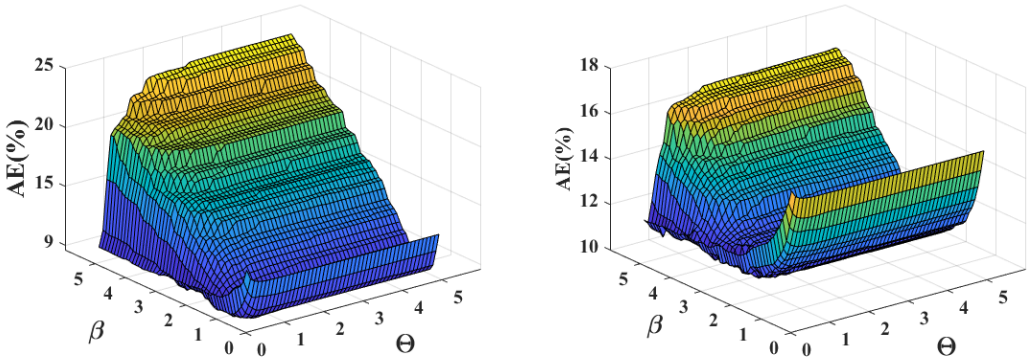

(a) CRF-WMM (b) CRF-GMM

Fig. 8: Detected oil spill candidates by using (a) the CRF-WMM model with $AE = 9.56\%$ and (b) the CRF-GMM with $AE = 11.29\%$. GC is used as the optimizer.

TABLE V: Values of the errors for the simulated full scene achieved by CRF-WMM and CRF-GMM using the GC optimization method.

	CE(%)	*OE*(%)	*AE*(%)
CRF-WMM	**4.51**	**14.61**	**9.56**
CRF-GMM	4.55	18.03	11.29

Numbers in **bold** indicate the lowest error using each of the optimization methods

achieved by CRF-GMM, and CRF-WMM models are shown in Table V, which are consistent with the visual detection results. The values of *AE* are 9.56% and 11.29% for CRF-WMM and CRF-GMM, which are almost 2% and 3% lower than those obtained by GC-WMM and GC-GMM, respectively.

Finally, to show the sensitivity of the proposed model to the values of β and θ, the grid search results obtained by CRF-WMM and CRF-GMM methods are illustrated in Figure 8. As can be seen, converging to the minimum of *AE* is straightforward because there are no saddle points and abrupt changes are not seen on the search surface. In other words, a small change in the values of β and θ does not result in a significant change in *AE*.

VII. Conclusion

This paper has presented a CRF-WMM algorithm tailored to the CP SAR statistics to utilize both the full CP information and the spatial context information in CP SAR imagery for enhanced oil spill candidate detection. First, to utilize the statistical properties of CP SAR data, we designed a unary potential based on the complex Wishart distribution. Second, to take advantage of contextual information, we included a similarity measure based on C^{22}. Theoretically, C^{22} is sensitive to the sea surface roughness and has a high signal-to-noise ratio. The empirical results prove that this similarity measure can improve the accuracy of detecting oil spill candidates. Finally, to solve the proposed ill-posed CRF model, we utilized three common optimization algorithms and compared their performance to specify the most appropriate optimization algorithm for detecting oil spill candidates in simulated RCM CP SAR data. The proposed approach is tested on both the simulated sub-images and the full scene. The results demonstrate that the proposed model can better delineate oil spill candidates than the traditional CRF and MRF approaches that do not consider the properties of the CP data. Overall, the proposed model can delineate oil spill candidates without being significantly affected by oil free water and oil spill heterogeneities. In addition, the number of false negatives in the CRF-WMM

model is much lower than that in the other approaches, meaning that using the proposed model can decrease the risk of misclassifying oil spill candidate pixels that will not be detected in oil spill classification methods. Considering that the four nearest neighbor pixels and C^{22} intensity image were used to model spatial context information, future research directions should investigate using larger spatial scales as well as other features such as decomposition parameters in detecting oil spill candidates.

REFERENCES

[1] B. Fiscella, A. Giancaspro, F. Nirchio, P. Pavese, and P. Trivero, "Oil spill detection using marine SAR images," *International Journal of Remote Sensing*, vol. 21, no. 18, pp. 3561–3566, 2000.

[2] D. Flett, Y. Crevier, and R. Girard, "The RADARSAT Constellation Mission: Meeting the government of canada's needs and requirements," in *2009 IEEE International Geoscience and Remote Sensing Symposium*, vol. 2. IEEE, 2009, pp. II–910.

[3] C. S. Agency, "Technical characteristics," 2020. [Online]. Available: https://www.asc-csa.gc.ca/eng/satellites/radarsat/technical-features/characteristics.asp

[4] R. K. Panigrahi and A. K. Mishra, "Comparison of hybrid-pol with quad-pol scheme based on polarimetric information content," *International journal of remote sensing*, vol. 33, no. 11, pp. 3531–3541, 2012.

[5] R. Raney, "Hybrid-polarity SAR architecture," in *2006 IEEE International Symposium on Geoscience and Remote Sensing*. IEEE, 2006, pp. 3846–3848.

[6] M. M. Espeseth, C. E. Jones, B. Holt, C. Brekke, and S. Skrunes, "Oil-spill-response-oriented information products derived from a rapid-repeat time series of SAR images," *IEEE Journal of Selected Topics in Applied Earth Observations and Remote Sensing*, vol. 13, pp. 3448–3461, 2020.

[7] Y. Shu, J. Li, H. Yousif, and G. Gomes, "Dark-spot detection from SAR intensity imagery with spatial density thresholding for oil-spill monitoring," *Remote Sensing of Environment*, vol. 114, no. 9, pp. 2026–2035, 2010.

[8] A. S. Solberg, G. Storvik, R. Solberg, and E. Volden, "Automatic detection of oil spills in ERS SAR images," *IEEE Transactions on geoscience and remote sensing*, vol. 37, no. 4, pp. 1916–1924, 1999.

[9] L. De Laurentiis, C. E. Jones, B. Holt, G. Schiavon, and F. Del Frate, "Deep learning for mineral and biogenic oil slick classification with airborne synthetic aperture radar data," *IEEE Transactions on Geoscience and Remote Sensing*, vol. 59, no. 10, pp. 8455–8469, 2020.

[10] C. Brekke and A. H. Solberg, "Oil spill detection by satellite remote sensing," *Remote sensing of environment*, vol. 95, no. 1, pp. 1–13, 2005.

[11] B. Minchew, C. E. Jones, and B. Holt, "Polarimetric analysis of backscatter from the deepwater horizon oil spill using L-band synthetic aperture radar," *IEEE Transactions on Geoscience and Remote Sensing*, vol. 50, no. 10, pp. 3812–3830, 2012.

[12] J.-S. Lee, M. R. Grunes, and G. De Grandi, "Polarimetric SAR speckle filtering and its implication for classification," *IEEE Transactions on Geoscience and remote sensing*, vol. 37, no. 5, pp. 2363–2373, 1999.

[13] J. R. Jensen, *Remote sensing of the environment: An earth resource perspective 2/e*. Pearson Education India, 2009.

[14] S. M. Ahmed, F. A. E. Eldin, and A. M. Tarek, "Speckle noise reduction in SAR images using adaptive morphological filter," in *2010 10th International Conference on Intelligent Systems Design and Applications*. IEEE, 2010, pp. 260–265.

[15] B. Zhang, W. Perrie, X. Li, and W. G. Pichel, "Mapping sea surface oil slicks using RADARSAT-2 quad-polarization SAR image," *Geophysical Research Letters*, vol. 38, no. 10, 2011.

[16] R. Shirvany, M. Chabert, and J.-Y. Tourneret, "Ship and oil-spill detection using the degree of polarization in linear and hybrid/compact dual-pol SAR," *IEEE Journal of Selected Topics in Applied Earth Observations and Remote Sensing*, vol. 5, no. 3, pp. 885–892, 2012.

[17] F. Nunziata, M. Migliaccio, and X. Li, "Sea oil slick observation using hybrid-polarity SAR architecture," *IEEE Journal of Oceanic Engineering*, vol. 40, no. 2, pp. 426–440, 2014.

[18] A.-B. Salberg, Ø. Rudjord, and A. H. S. Solberg, "Oil spill detection in hybrid-polarimetric SAR images," *IEEE Transactions on Geoscience and Remote Sensing*, vol. 52, no. 10, pp. 6521–6533, 2014.

[19] J. Lafferty, A. McCallum, and F. C. Pereira, "Conditional random fields: Probabilistic models for segmenting and labeling sequence data," 2001.

[20] T. Liu, X. Huang, and J. Ma, "Conditional random fields for image labeling," *Mathematical Problems in Engineering*, vol. 2016, 2016.

[21] M. J. Collins, M. Denbina, B. Minchew, C. E. Jones, and B. Holt, "On the use of simulated airborne compact polarimetric sar for characterizing oil–water mixing of the deepwater horizon oil spill," *IEEE Journal of Selected Topics in Applied Earth Observations and Remote Sensing*, vol. 8, no. 3, pp. 1062–1077, 2015.

[22] C. Elachi, "Spaceborne imaging radar: geologic and oceanographic applications," *Science*, vol. 209, no. 4461, pp. 1073–1082, 1980.

[23] A. H. S. Solberg and E. Volden, "Incorporation of prior knowledge in automatic classification of oil spills in ers sar images," in *IGARSS'97. 1997 IEEE International Geoscience and Remote Sensing Symposium Proceedings. Remote Sensing-A Scientific Vision for Sustainable Development*, vol. 1. IEEE, 1997, pp. 157–159.

[24] H. Espedal, "Satellite sar oil spill detection using wind history information," *International Journal of Remote Sensing*, vol. 20, no. 1, pp. 49–65, 1999.

[25] H. Espedal and O. Johannessen, "Cover: detection of oil spills near offshore installations using synthetic aperture radar (sar)," 2000.

[26] L. Xu, J. Li, and A. Brenning, "A comparative study of different classification techniques for marine oil spill identification using radarsat-1 imagery," *Remote Sensing of Environment*, vol. 141, pp. 14–23, 2014.

[27] A. Gambardella, M. Migliaccio, and G. De Grandi, "Wavelet polarimetric sar signature analysis of sea oil spills and look-alike features," in *2007 IEEE International Geoscience and Remote Sensing Symposium*. IEEE, 2007, pp. 983–986.

[28] V. V. Malinovsky, S. Sandven, A. S. Mironov, and A. E. Korinenko, "Identification of oil spills based on ratio of alternating polarization images from envisat," in *2007 IEEE International Geoscience and Remote Sensing Symposium*. IEEE, 2007, pp. 1326–1329.

[29] M. Migliaccio, A. Gambardella, and M. Tranfaglia, "Sar polarimetry to observe oil spills," *IEEE Transactions on Geoscience and Remote Sensing*, vol. 45, no. 2, pp. 506–511, 2007.

[30] M. Migliaccio, F. Nunziata, and A. Gambardella, "On the co-polarized phase difference for oil spill observation," *International Journal of Remote Sensing*, vol. 30, no. 6, pp. 1587–1602, 2009.

[31] P. C. Genovez, C. E. Jones, S. J. Sant'Anna, and C. C. Freitas, "Oil slick characterization using a statistical region-based classifier applied to uavsar data," *Journal of Marine Science and Engineering*, vol. 7, no. 2, p. 36, 2019.

[32] S. Skrunes, C. Brekke, and T. Eltoft, "Characterization of marine surface slicks by radarsat-2 multipolarization features," *IEEE Transactions on Geoscience and Remote Sensing*, vol. 52, no. 9, pp. 5302–5319, 2013.

[33] L. Xu, M. Javad Shafiee, A. Wong, F. Li, L. Wang, and D. Clausi, "Oil spill candidate detection from sar imagery using a thresholding-guided stochastic fully-connected conditional random field model," in *Proceedings of the IEEE Conference on Computer Vision and Pattern Recognition Workshops*, 2015, pp. 79–86.

[34] D. I. Morales, M. Moctezuma, and F. Parmiggiani, "Detection of oil slicks in sar images using hierarchical mrf," in *IGARSS 2008-2008 IEEE International Geoscience and Remote Sensing Symposium*, vol. 3. IEEE, 2008, pp. III–1390.

[35] S. Pelizzari and J. Bioucas-Dias, "Oil spill segmentation of sar images via graph cuts," in *2007 IEEE International Geoscience and Remote Sensing Symposium*. IEEE, 2007, pp. 1318–1321.

[36] S. Martinis, "Automatic oil spill detection in terrasar-x data using multi-contextual markov modeling on irregular graphs," in *2012 3rd International Conference on Image Processing Theory, Tools and Applications (IPTA)*. IEEE, 2012, pp. 43–46.

[37] F. Parmiggiani, L. Alvarez-Hernandez, and M. Moctezuma-Flores, "A stochastic model for oil spill detection in marine environment with sar data," in *Remote Sensing of the Ocean, Sea Ice, Coastal Waters, and Large Water Regions 2018*, vol. 10784. SPIE, 2018, pp. 111–116.

[38] H. Guo, D. Wu, and J. An, "Discrimination of oil slicks and lookalikes in polarimetric sar images using cnn," *Sensors*, vol. 17, no. 8, p. 1837, 2017.

[39] X. Yaohua and M. Xudong, "A sar oil spill image recognition method based on densenet convolutional neural network," in *2019 International Conference on Robots & Intelligent System (ICRIS)*. IEEE, 2019, pp. 78–81.

[40] H. Li, W. Perrie, and J. Wu, "Retrieval of oil–water mixture ratio at ocean surface using compact polarimetry synthetic aperture radar," *Remote Sensing*, vol. 11, no. 7, p. 816, 2019.

[41] Y. Li, Y. Zhang, J. Chen, and H. Zhang, "Improved compact polarimetric sar quad-pol reconstruction algorithm for oil spill detection," *IEEE geoscience and remote sensing letters*, vol. 11, no. 6, pp. 1139–1142, 2013.

[42] M. M. Espeseth, S. Skrunes, C. E. Jones, C. Brekke, B. Holt, and A. P. Doulgeris, "Analysis of evolving oil spills in full-polarimetric and hybrid-polarity sar," *IEEE Transactions on Geoscience and Remote Sensing*, vol. 55, no. 7, pp. 4190–4210, 2017.

[43] B. Minchew, "Determining the mixing of oil and sea water using polarimetric synthetic aperture radar," *Geophysical Research Letters*, vol. 39, no. 16, 2012.

[44] V. Chaudhary and S. Kumar, "Marine oil slicks detection using space-borne and airborne sar data," *Advances in Space Research*, vol. 66, no. 4, pp. 854–872, 2020.

[45] J. J. van Zyl, M. Arii, and Y. Kim, "Model-based decomposition of polarimetric sar covariance matrices constrained for nonnegative eigenvalues," *IEEE Transactions on Geoscience and Remote Sensing*, vol. 49, no. 9, pp. 3452–3459, 2011.

[46] S. R. Cloude, D. G. Goodenough, and H. Chen, "Compact decomposition theory," *IEEE Geoscience and Remote Sensing Letters*, vol. 9, no. 1, pp. 28–32, 2011.

[47] V. Chaudhary and S. Kumar, "Dark spot detection for characterization of marine surface slicks using uavsar quad-pol data," *Scientific Reports*, vol. 11, no. 1, p. 8975, 2021.

[48] H. Li, W. Perrie, Y. He, J. Wu, and X. Luo, "Analysis of the polarimetric sar scattering properties of oil-covered waters," *IEEE Journal of Selected Topics in Applied Earth Observations and Remote Sensing*, vol. 8, no. 8, pp. 3751–3759, 2014.

[49] R. K. Raney, J. T. Cahill, G. W. Patterson, and D. B. J. Bussey, "The m-chi decomposition of hybrid dual-polarimetric radar data with application to lunar craters," *Journal of Geophysical Research: Planets*, vol. 117, no. E12, 2012.

[50] Y. Wu, K. Ji, W. Yu, and Y. Su, "Region-based classification of polarimetric sar images using wishart mrf," *IEEE Geoscience and Remote Sensing Letters*, vol. 5, no. 4, pp. 668–672, 2008.

[51] A. Stumpf and N. Kerle, "Combining random forests and object-oriented analysis for landslide mapping from very high resolution imagery," *Procedia Environmental Sciences*, vol. 3, pp. 123–129, 2011.

[52] M. Moctezuma and F. Parmiggiani, "Adaptive stochastic minimization for measuring marine oil spill extent in synthetic aperture radar images," *Journal of Applied Remote Sensing*, vol. 8, no. 1, pp. 083 553–083 553, 2014.

[53] G. Atteia and M. J. Collins, "On the use of compact polarimetry sar for ship detection," *ISPRS Journal of Photogrammetry and Remote Sensing*, vol. 80, pp. 1–9, 2013.

[54] R. K. Raney, "Comparing compact and quadrature polarimetric sar performance," *IEEE Geoscience and Remote Sensing Letters*, vol. 13, no. 6, pp. 861–864, 2016.

[55] ——, "Hybrid-polarity sar architecture," *IEEE Transactions on Geoscience and Remote Sensing*, vol. 45, no. 11, pp. 3397–3404, 2007.

[56] C. Brekke, C. E. Jones, S. Skrunes, B. Holt, M. Espeseth, and T. Eltoft, "Cross-correlation between polarization channels in sar imagery over oceanographic features," *IEEE Geoscience and remote sensing letters*, vol. 13, no. 7, pp. 997–1001, 2016.

[57] G. Gao, S. Gao, J. He, and G. Li, "Ship detection using compact polarimetric SAR based on the notch filter," *IEEE Transactions on Geoscience and Remote Sensing*, vol. 56, no. 9, pp. 5380–5393, 2018.

[58] Q. Yu and D. A. Clausi, "IRGS: Image segmentation using edge penalties and region growing," *IEEE transactions on pattern analysis and machine intelligence*, vol. 30, no. 12, pp. 2126–2139, 2008.

[59] X. Deng, C. López-Martínez, J. Chen, and P. Han, "Statistical modeling of polarimetric SAR data: A survey and challenges," *Remote Sensing*, vol. 9, no. 4, p. 348, 2017.

[60] J.-S. Lee and E. Pottier, *Polarimetric radar imaging: from basics to applications*. CRC press, 2017.

[61] C. Oliver and S. Quegan, *Understanding synthetic aperture radar images*. SciTech Publishing, 2004.

[62] J.-S. Lee, M. R. Grunes, and R. Kwok, "Classification of multi-look polarimetric sar imagery based on complex wishart distribution," *International Journal of Remote Sensing*, vol. 15, no. 11, pp. 2299–2311, 1994.

[63] W. Xie, Z. Xie, F. Zhao, and B. Ren, "Polsar image classification via clustering-wae classification model," *IEEE Access*, vol. 6, pp. 40 041–40 049, 2018.

[64] E. Goumehei, V. Tolpekin, A. Stein, and W. Yan, "Surface water body detection in polarimetric sar data using contextual complex wishart classification," *Water resources research*, vol. 55, no. 8, pp. 7047–7059, 2019.

[65] J. Besag, "On the statistical analysis of dirty pictures," *Journal of the Royal Statistical Society: Series B (Methodological)*, vol. 48, no. 3, pp. 259–279, 1986.

[66] S. Geman and D. Geman, "Stochastic relaxation, gibbs distributions, and the bayesian restoration of images," *IEEE Transactions on pattern analysis and machine intelligence*, no. 6, pp. 721–741, 1984.

[67] V. Kolmogorov and R. Zabin, "What energy functions can be minimized via graph cuts?" *IEEE transactions on pattern analysis and machine intelligence*, vol. 26, no. 2, pp. 147–159, 2004.

[68] N. R. Goodman, "Statistical analysis based on a certain multivariate complex gaussian distribution (an introduction)," *The Annals of mathematical statistics*, vol. 34, no. 1, pp. 152–177, 1963.

[69] H. Derin and H. Elliott, "Modeling and segmentation of noisy and textured images using gibbs random fields," *IEEE Transactions on pattern analysis and machine intelligence*, no. 1, pp. 39–55, 1987.

[70] Y. Li, H. Lin, Y. Zhang, and J. Chen, "Comparisons of circular transmit and linear receive compact polarimetric sar features for oil slicks discrimination," *Journal of Sensors*, vol. 2015, 2015.

[71] A. Cheng, M. Arkett, T. Zagon, R. De Abreu, D. Mueller, P. Vachon, and J. Wolfe, "Oil detection in radarsat-2 quad-polarization imagery: Implications for scansar performance," in *SAR Image Analysis, Modeling, and Techniques XI*, vol. 8179. SPIE, 2011, pp. 119–133.

[72] F. Charbonneau, B. Brisco, R. Raney, H. McNairn, C. Liu, P. Vachon, J. Shang, R. DeAbreu, C. Champagne, A. Merzouki *et al.*, "Compact polarimetry overview and applications assessment," *Canadian Journal of Remote Sensing*, vol. 36, no. sup2, pp. S298–S315, 2010.

[73] Z. Zivkovic, "Gentle icm energy minimization for markov random fields with smoothness-based priors," *Journal of Real-Time Image Processing*, vol. 11, no. 1, pp. 235–246, 2016.

[74] Y. Boykov and O. Veksler, "Graph cuts in vision and graphics: Theories and applications," in *Handbook of mathematical models in computer vision*. Springer, 2006, pp. 79–96.